Numerical simulation of the General Circulation of the atmosphere of Titan

Frédéric Hourdin, Olivier Talagrand, Robert Sadourny,
Laboratoire de Météorologie Dynamique du CNRS
Ecole Normale Supérieure/ 24 rue Lhomond/ 75231 PARIS cedex 05/ FRANCE
FAX: 33-1-43-36-83-92/ e-mail: hourdin@lmd.ens.fr

Régis Courtin, Daniel Gautier,
DESPA/Obs Paris Meudon/92 190 Meudon/FRANCE

Christopher P. McKay
NASA Ames Research Center
Moffett Field, CA 94035

23 pages, 0 tables and 14 figures
Submitted to *Icarus*

September 27, 1994

Proposed running head:

General circulation of the atmosphere of Titan

The correspondence should be directed to:

Frédéric Hourdin

Laboratoire de Météorologie Dynamique du CNRS
Ecole Normale Supérieure
24 rue Lhomond
75231 PARIS cedex 05
FRANCE

FAX: 33-1-43-36-83-92
e-mail: hourdin@lmd.ens.fr

Abstract

The atmospheric circulation of Titan is investigated with a general circulation model. The representation of the large scale dynamics is based on a grid point model developed and used at Laboratoire de Météorologie Dynamique for climate studies. The code also includes an accurate representation of radiative heating and cooling by molecular gases and haze has well as a parametrization of the vertical turbulent mixing of momentum and potential temperature. Long term simulations of the atmospheric circulation are presented. Starting from a state of rest, the model spontaneously produces a strong superrotation with prograde equatorial winds (*i. e.* in the same sense as the assumed rotation of the solid body) increasing from the surface to reach 100 ms^{-1} near the 1 mbar pressure level. Those equatorial winds are in very good agreement with some indirect observations, especially those of the occultation of the 28-Sgr by Titan. On the other hand, the model simulates latitudinal temperature contrasts in the stratosphere significantly weaker than those observed by Voyager 1 which, we suggest, may be partly due to the non-representation of the spatial and temporal variations of the abundances of molecular species and haze. We present diagnostics of the simulated atmospheric circulation underlying the importance of the seasonal cycle and a tentative explanation for the creation and maintenance of the atmospheric superrotation based on a careful angular momentum budget.

1 Introduction

Titan, the largest moon of Saturn, is unique among the moons of the solar system in that it has a thick atmosphere. Titan has a radius of 2575 km and appears to be synchronously locked implying a prograde rotation rate equal to its orbit about Saturn of $\simeq$ 16 days. Due to Saturn's obliquity of 26.7° Titan experiences seasonal changes over the Saturnian year of $\simeq$ 30 terrestrial years (Hunten et al., 1984) . Titan's atmosphere has a surface pressure and temperature of $\simeq$ 1.5 atms and 95 K, respectively (Lindal et al., 1983) near the equator. The temperature decreases above the surface reaching a minimum of $\simeq$ 71 K at 40 km before increasing again to $\simeq$ 170 K at the 1 mb level (Lellouch et al., 1989) . The dominant gas is N_2 (Broadfoot et al., 1981) with a few percent CH_4 in the stratosphere (Lellouch et al., 1989) , $\simeq$ 0.2% H_2 (Samuelson et al., 1981) , trace hydrocarbons (Kunde et al., 1981) , and an uncertain level of Ar, $\leq$ 10% (Strobel et al., 1993) . A high altitude haze is observed on Titan that is optically thick in the visible (Rages and Pollack, 1983; Rages et al., 1983) obscuring the surface and lower atmosphere. This haze is thought to be composed of organic solids produced by photochemical reactions in the upper atmosphere (see e.g. Khare et al., 1984; Sagan and Thompson, 1984) . The reflectivity of this haze varies with time of year (Lockwood, 1977; Lockwood et al., 1986) and it exhibited an hemispheric dichotomy when Voyager flew by Titan in 1980 (Sromovsky et al., 1981) . The connection between the temporal variations and the hemispheric contrast (suggested by Sromovsky et al., 1981) was confirmed by observations with the Hubble Space Telescope (Caldwell et al., 1992) .

The question we address in this paper is the nature of the atmospheric circulation on such a world.

Early work on the circulation of Titan's atmosphere deduced that horizontal temperature variations in the lower atmosphere would be small and it was suggested that the circulation would fall in the symmetric rather than wave regime (Leovy et al., 1973; Golitsyn, 1975) being more analogous to Venus than Mars or Earth. Golitsyn (1975) was the first to suggest that, like Venus, Titan may have superrotation in its upper atmosphere. The first evidence, albeit indirect, of circulation on Titan came from the

Voyager observations. It was suggested that the latitudinal difference in the haze reflectance could be due to circulation (Sromovsky et al., 1981) . Flasar et al. (1981) also inferred a possible circulation from the temperature data and suggested superrotation in the upper atmosphere. In addition to equator-to-pole temperature gradients, the Voyager data clearly indicated a hemispherical asymmetry at the 0.4 and 1 mb level. Flasar and Conrath (1990) deduced from this temperature contrast that the circulation lags the solar forcing. However, asymmetries in the radiative heating and cooling rates due to hemispheric asymmetries in the atmospheric composition and haze (Coustenis and Bézard, 1994) are large enough to explain the observed temperature contrast alone (Bezard et al., 1994) – although this does not preclude dynamics from playing an important role.

Evidence for circulation and superrotation was derived from stellar occultation by (Sicardy et al., 1990) who suggested that Titan's atmosphere at the 250 km level rotated in $\geq$ 26 h (see also Hubbard, 1993) . Early work on General Circulation Models (GCM) of Titan supported the idea of superrotation (Hourdin et al., 1992) as did studies based on a simplified Earth GCM with Titan-like rotation rates (Del Genio et al., 1993) . In this paper we continue our investigation of Titan's circulation and possible superrotation using a GCM originally developed for terrestrial applications but also applicable to other planetary atmospheres.

The adaptation of Terrestrial GCMs for other Earth-like planetary atmospheres has been particularly successful in the last decades for our understanding of the climate of Mars (Pollack et al., 1981; Pollack et al., 1993; Haberle et al., 1993; Barnes et al., 1993; Hourdin et al., 1993; Hourdin et al., 1994) . On the opposite, no GCM has yet simulated a realistic Venusian circulation. The only GCMs to have succeeded in creating a strong atmospheric superrotation in Venusian conditions were affected by unrealistic sources of angular momentum due for instance to a strong horizontal diffusion (Young and Pollack, 1990) or to the non-conservation of angular momentum by the numerical scheme Tourte (1984). On the other hand recent studies have succeeded in a more general context to simulate a strong atmospheric superrotation with GCMs for slowly rotating planets with large deposition of visible radiation in the atmosphere (which increases the vertical static stability of the atmosphere). The first successful attempt was that by Hourdin et al. (1992), based on the use of a simplified physical parametrization, in which the description of the planet is reduced to a set of 19 parameters (this work is described in more details by Hourdin and Talagrand, 1994) . The other study was conducted by Del Genio et al. (1993) with a "dry" version of the NASA/GISS Terrestrial GCM.

The Titan model used in the present paper (described in Section 2) has been adapted from the terrestrial atmospheric GCM developed at LMD for climate studies. It utilizes the same dynamical code, based on the classical primitive equations of meteorology (see e.g. Holton, 1979) , and the same parametrization for vertical turbulent mixing, horizontal dissipation and convection. The radiative transfer is computed with the code developed for Titan by McKay et al. (1989). The simulations performed with this model are presented in Section 3. One key result of those simulations, performed starting from an atmosphere at rest, is the creation of a strong atmospheric superrotation, of the same order of magnitude as that deduced from various indirect observations (with prograde zonal winds near 1 mbar of the order of 100 m s^{-1}). Comparisons to available observations are discussed in Section 4 as well as a tentative explanation for the creation and maintenance of the atmospheric superrotation. As for the more theoretical simulations of superrotation mentioned previously, the upward transport of angular momentum by the mean meridional Hadley circulation and equatorward transport by eddies play a key role for the creation and maintenance of superrotation, as already proposed by Gierasch (1975).

2 Model description

For now five years, the LMD terrestrial atmospheric GCM has been adapted successively to various planetary conditions. All versions use the same code for the explicit representation of large scale dynamics (based on a finite-difference representation of the primitive equations of meteorology), for horizontal dissipation (needed both for model stability and to account for the interaction between resolved and subgrid-scale motions) and for vertical turbulent mixing. In fact, three planetary versions were developed which essentially differ one from another by their radiative heating codes: one for Mars, fully described by Hourdin *et al.* (1993), for which a specific radiative scheme was developed (Hourdin, 1992) , the version for Titan (this paper) based on the use of the radiative code developed by McKay et al. (1989), and a more general version, based on the use of a simplified radiative forcing, in which the description of the planet is reduced to a set of 19 parameters. This last version was used in a theoretical study of atmospheric superrotation (Hourdin and Talagrand, 1994) .

2.1 Dynamics

The dynamical part of the code is based on a finite-difference formulation of the primitive equations of meteorology developed by R. Sadourny (see e. g. Sadourny and Laval, 1984) and coded in FORTRAN 77 by P. Le Van. The dynamics conserve exactly mass, potential temperature and its square for adiabatic motion, potential vorticity for barotropic motions (Sadourny, 1975b; Sadourny, 1975a) and angular momentum for axi-symmetric flows (Hourdin and Talagrand, 1994) . The conservation of angular momentum is essential to insure that a simulated superrotation is not produced by an artificial numerical source. This was checked in the simulation of atmospheric superrotation performed with the 19 parameters general circulation model (Hourdin and Talagrand, 1994) . The dynamical equations are based on a staggered latitude-longitude Arakawa C-grid (see *e. g.*, Kasahara, 1977) .

2.2 Horizontal dissipation

Almost all GCMs introduce a kind of "super-viscosity" to account for the nonlinear interaction between explicitly resolved scales (typically of the order of a few hundred kilometers) and subgrid-scale motions. Such a dissipation is also generally needed for model stability. This is particularly true for the LMD GCM, the formulation of which is designed to correctly represent the enstrophy cascade[1] since potential enstrophy is

---

[1] Theory of the horizontal 2-D turbulence suggests that enstrophy – square of the wind rotational – is pumped from the large scales at which it is generated toward small scales until dissipation at

exactly conserved by the finite-difference formulation. Since the enstrophy cascade can not propagate beyond the smallest scale of the model, it would naturally result in an accumulation of enstrophy at the grid-scale and finally produce dynamical unstabilities. Therefore, an horizontal dissipation operator is introduced in the LMD GCM, based on a Laplacian operator, specially designed to selectively remove enstrophy but not energy at the grid-scale. The Laplacian is iterated in order to be more selective in the smallest model scales. In the simulations presented here, the operator was iterated two times.

Note that some models are stable without super-viscosity, but it means that the numerical scheme for explicitly resolved motions itself provides enstrophy dissipation at small scales. The drawback of such a model is that this dissipation is not totally under control.

2.3 Radiative forcing

Because seasons and radiative time constants are much longer on Titan than the dynamical time-step of our model (of the order of a few minutes) the problem of numerical efficiency is not so crucial as on Mars for instance. Therefore, to compute the radiative forcing we utilize directly the solar heating and radiative cooling rates determined with the spectrally resolved radiative model developed and described by McKay *et al.* (1989,1991,1993). The model has 24 solar spectral intervals and 46 in the thermal infrared. The radiative transfer equation for both the solar and thermal infrared is solved by different variants of the two stream approximation (Toon et al. 1989). The atmosphere is subdivided into layers within which all material properties are assumed to be constant and the temperature is assumed to vary linearly. In the visible there is scattering and absorption by the haze, Rayleigh scattering by the atmosphere, and absorption by CH_4. The thermal infrared opacity in the lower atmosphere is dominated by collision induced absorption by N_2, CH_4, and H_2 (Courtin 1988, McKay *et al.* , 1989, 1991). In the stratosphere emission by the haze and organic molecules are

---

molecular scales (see *e. g.*,Pedlosky, 1982) important cooling sources. A semi-analytic model of the haze is used to compute the haze properties given the production rate and electrostatic charging factor (McKay *et al.* , 1989). The incoming solar radiation is strongly absorbed in the stratosphere by haze particles and by CH_4. Globally averaged, about 40% of the solar radiation is absorbed in the stratosphere, 30% is absorbed below the tropopause (10% reaches the surface); the remaining 30% is reflected to space (McKay *et al.* , 1991).

The model contains a number of free parameters: such as the haze production rate and the mixing ratio of H_2. Values for these parameters are selected based upon spacecraft and Earth-based observations of Titan (McKay *et al.* , 1989). There is sufficient data that all parameters can be chosen independent of the observed thermal profile. Adjustments of the model parameters within the limits allowed by the data are sufficient to bring the 1-D temperature profile computed with a radiative convective approach into agreement with the *Voyager 1* results (McKay et al., 1993) .

In computing the radiative forcing as a function of latitude we have assumed that the mole fractions of absorbing and emitting gases depend only on altitude, not latitude or season. The haze production rate and optical properties are also assumed to be independent of time and location. For the aerosols this is certainly an oversimplification since there are observed hemispherical and seasonal changes in Titan's albedo that are related to the haze concentration for properties. Preliminary studies by Hutzell et al. (1994). suggest that these can be explained as a result of transport of haze particles by atmospheric winds.

2.4 Other physics

The effect of turbulent mixing on both potential temperature ($\theta = T\,(p_S/p)^{\kappa}$) and momentum is computed as

$$\frac{\partial q}{\partial t} = \frac{1}{\rho}\frac{\partial}{\partial z}\left(\rho K_z \frac{\partial q}{\partial z}\right) \qquad (1)$$

As in the original terrestrial version, the turbulent mixing coefficient K_z is computed as $K_z = l e^{1/2}$ in terms of mixing length l and a diagnostic estimate of the turbulent kinetic energy

$$e = Max\left[l^2\left\|\frac{\partial\vec{V}}{\partial z}\right\|^2(1 - Ri/Ri_c), e_{min}\right] \tag{2}$$

where Ri is the Richardson number

$$Ri = \frac{g\partial\theta/\partial z}{\theta\left(\partial\vec{V}/\partial z\right)^2}. \tag{3}$$

The surface drag coefficient is just fixed as a constant in the simulation. The occurrence of vertical unstable temperature profiles ($Ri < 0$) is prevented using a simple dry convective adjustment with partial momentum mixing depending on the strength of the vertical unstability (see Hourdin et al., 1993) . Finally, the time evolution of the surface temperature is computed by dividing the net surface flux (radiation plus sensible heat flux) by a single heat surface capacity.

2.5 Grid

For the present study, we use two different horizontal resolutions: a low resolution based on 32 longitudes and 24 latitudes and a high resolution based on twice more points in each direction. In both cases, points are equally spaced in longitude and latitude. The vertical discretization is based on 55 σ-levels (σ is the pressure normalized to its surface value which is commonly used as a vertical coordinate in general circulation models) almost equally spaced in log-pressure except near the bottom and top of the atmosphere – a simulation was also performed with the low horizontal resolution and 100 layers on the vertical –. In term of altitude, the layers are typically 2.5 km thick in the troposphere against 9 km in the stratosphere which corresponds to about 5 layers per atmospheric scale height.

Since dynamics are integrated explicitly in time, the time-step is limited by a CFL criterion. It was empirically fixed to 400 s for the coarse horizontal resolution and 180 s for the high resolution.

3 Numerical simulations

3.1 Radiative-convective simulation

A preliminary experiment has been performed with a two-dimensional (latitude–pressure) version of the model (with 48 points in latitude and 55 points on the vertical) in which only the temperature field was varied under the effect of radiative heating and convective adjustment. The model was started from an isothermal ($T = 120$ K) atmosphere and integrated over 10 Titan years taking into account the seasonal variations of insolation.

The temperature for northern winter solstice and spring equinox of year 10 of the simulation are shown in Fig. 1.

[Figure 1 about here.]

There is a clear difference between the stratosphere, where, because of short radiative time constants, the temperature structure is in phase with insolation (symmetric at equinox) and the troposphere, where the thermal structure lags insolation by more than half a season. Note however, that, even in the stratosphere, the thermal structure is not exactly symmetric at northern spring equinox, time of the Voyager encounter.

In the current model version, the time evolution of the surface temperature is crudely computed from the surface energy budget (including radiation and sensible heat fluxes) using a single layer soil characterized by its heat surface capacity. The value of this capacity (5×10^5 J m^{-2} K^{-1}) is taken from the LMD terrestrial GCM and accounts for the response of soil temperature to synoptic perturbations. Thus the adjusting time of the surface temperature is much shorter than one Titan season.

In order to test the possible impact of this assumption, we performed another simulation by replacing the simple surface heat balance computation by a complete 11-layer model of thermal conduction in the soil with a large thermal inertia (30 000 J m^{-2} s$^{-1/2}$ K^{-1}) corresponding to terrestrial oceans (for comparison, the thermal inertia of terrestrial solid surface is typically of the order of 2000 J m^{-2} s$^{-1/2}$ K^{-1}). The temperature is not affected by this change except near the surface (between 1440 and 1000 mbar) where the structure is more symmetric during the whole year with a phase lag close to one season.

3.2 Spin-up phase

A first three-dimensional dynamical simulation was performed over 23 Titan years with the low horizontal resolution and 55 levels on the vertical. The simulation was started from a state of rest with no horizontal temperature variations and the vertical Lellouch temperature profile (Lellouch et al., 1989) .

In this simulation, the ellipticity of the Titan orbit around sun was neglected in order to make the two hemispheres equivalent. Titan was assumed to be in synchronous orbit around Saturn. We used typical terrestrial values (taken from the LMD climate GCM) for the critical Richardson number ($Ri_c = 0.4$), for the vertical turbulent mixing length $l = 35$ m and for the surface drag coefficient $C_D = 10^{-3}$. The minimum turbulent kinetic energy was fixed to $e_{min} = 10^{-12}$ m^2 s^{-2} (leading to a minimum value of the mixing coefficient $K_z = 3.5 \times 10^{-5}$ m^2 s^{-1} for large Richardson numbers). Test simulations performed with a larger value of this minimum mixing coefficient were found to produce a significant deterioration of the global vertical temperature profile. The diurnal cycle was also intentionally turned off in this first numerical experiment in order to save CPU hours. The radiative transfer was only computed three times per Titan day.

[Figure 2 about here.]

The most remarkable result of this first simulation is the fact that the circulation, after a long spin-up phase, reaches a regime of strong superrotation. Fig. 2 shows for four atmospheric layers – surface to 200 mbar (troposphere), 200 to 20 mbar (tropopause), 20 to 2 mbar (lower stratosphere) and 2 mbar to the atmospheric top (upper stratosphere) – the time evolution of the planetary averaged dimensionless angular momentum defined as the ratio of the specific angular momentum $a\cos\phi\,(u + a\Omega\cos\phi)$ to the mean specific angular momentum of the atmosphere at rest $2/3a^2\Omega$. The planetary average of this dimensionless angular momentum is an index of superrotation. At the end of the simulation, this superrotation index is of the order of 6 in the upper stratosphere, which just means that the atmosphere, at this level, rotates 6 times faster than the solid planet in term of mean angular momentum.

The short period oscillations in Fig. 2 correspond to seasonal variations of the mean angular momentum, with two maxima and two minima per year. In the upper atmospheric shell the superrotation index is minimum between solstice and equinox, increases to reach a maximum between equinox and solstice and then decreases again. These seasonal variations of the stratospheric angular momentum are discussed later on.

In order to reach a steady state regime, we started a new simulation by taking a state near the end of the first simulation and increasing the winds by 25%. A correction was also done on the temperature field in order to start not too far from thermal wind balance. The superrotation for that new simulation is also shown in Fig. 2. The superrotation index seems to be stabilized near 7 in the upper layer but still slightly increases in the rest of the atmosphere.

3.3 Sensitivity to the model spatial resolution

Two experiments were conducted in order to test the impact of the poor spatial model resolution on the numerical results, the first one by using twice more points in each horizontal direction (64 × 48 versus 32 × 24) and the second one by increasing the number of vertical layers from 55 to 100. Both tests were performed over a few Titan years starting from a state near the end of the control simulation (year 23).

[Figure 3 about here.]

An increase in the vertical resolution has almost no effect on the numerical results. An increase in the horizontal resolution does not affect either the tropospheric circulation nor the general pattern of the stratospheric circulation. However, this high resolution simulation significantly enhances the stratospheric superrotation as illustrated in Fig. 3. After 1.5 Titan years, the upper stratosphere rotates about 9 times faster than the solid planet and this superrotation still increases at the end of the simulation. This high resolution simulation, for which the insolation was now computed with a full diurnal cycle, is used for analyses later on.

3.4 Mean atmospheric state

Meridional circulation

[Figure 4 about here.]

As expected for slowly rotating planets absorbing more energy in tropical regions than in high latitudes – on an annual basis –, the annually and zonally averaged meridional circulation is dominated by large equator-to-pole cells (Fig. 4).

[Figure 5 about here.]

However, this mean pattern hides strong seasonal contrasts. Near solstice (upper panel of Fig. 5), the zonally averaged meridional circulation is dominated by a global pole-to-pole Hadley cell, the ascending branch of which is located in the summer hemisphere and the descending branch in the winter hemisphere. In fact, this global Hadley circulation persists during the main part of the time separating two consecutive equinoxes (from $L_S = 210$ to 330 for the northern winter for instance[2]) at least in the stratosphere. Note that the meridional wind at this season is northward above 10 mbar and below 30 mbar but southward between those two pressure levels. Therefore, the pattern of the mean meridional circulation at solstice can be interpreted as the superposition of two pole-to-pole direct Hadley cells, a tropospheric cell and a stratospheric cell centered at about 10 mbar.

Near equinox (lower panel of Fig. 5), the ascending branch of the mean meridional circulation moves from one pole to the other. At equinox itself, the stratospheric mean meridional circulation is characterized by two symmetric Hadley cells, one in each hemisphere, with equatorial ascending motions suggesting a fast response of the

---

[2] Here, L_S is the longitude of the sun in Saturn centered coordinates with $L_S = 0$ at Titan northern spring equinox.

stratospheric mean meridional circulation to the variations of insolation (the meridional circulation is symmetric from hemisphere to hemisphere when insolation is symmetric). The picture is different in the lower troposphere, below the 1000 mbar level: the ascending motions, near the surface, are located in the hemisphere coming out of summer (here the southern hemisphere), at about -30° latitude, and there are two cells in the hemisphere coming out of winter, a direct one in the tropics and mid latitudes and an indirect one at high latitudes. The radiative-convective simulations presented above suggest that this tropospheric mean meridional circulation could be affected significantly by the presence of global or large scale oceans.

Temperature

[Figure 6 about here.]

The vertical profile of the planetary averaged atmospheric temperature is shown in Fig. 6. Note that parameters of the radiative transfer model have been adjusted slightly to give agreement between the computed surface temperature and the Lellouch et al. (1989) results (McKay *et al.* 1989). However, there is a persistent difference between our results and the observations in the 1 mb region (see also McKay *et al.* 1989, 1991). The model results are about 10 K colder than the observations. While, the uncertainty in the derived temperature profile in this region is about 10 K (Lellouch *et al.* 1989) the model may well overestimate the radiative cooling or underestimate the solar heating in this region.

[Figure 7 about here.]

The latitudinal temperature variations (Fig. 7) are much weaker than in the radiative-convective simulation (Fig. 1). This result is not surprising since large scale dynamics, forced by the latitudinal variations of insolation, generally tend to reduce the latitudinal temperature contrasts by transporting energy from excess toward deficit regions. Moreover, numerical results (Del Genio et al., 1983) suggest that the latitudinal energy transport is more efficient for slowly rotating planets. The largest equator-to-pole temperature difference, about 22 K, is reached at solstice, in the winter hemisphere, for pressure levels between 15 and 5 mbar. The most puzzling result, as far as temperature are concerned, is the inversion of the latitudinal temperature gradient above 1 mbar, both at equinox and solstice (note that this result is independent of both the horizontal and vertical resolution).

Zonal wind

[Figure 8 about here.]

The zonally averaged zonal wind at the end of the high resolution simulation is shown in Fig. 8, both for northern winter solstice and spring equinox. The zonal wind is rather similar for those two seasons. Except near the surface where both eastward (in high latitudes) and westward (in low latitudes) winds occur, the atmosphere rotates faster than the solid planet everywhere ($u > 0$). The wind velocity increases strongly with altitude, especially above the 20 mbar level, to reach its maximum value near 1 mbar. The latitudinal structure is rather symmetric about the equator below 20 mbar, but asymmetric above. At solstice, the strongest winds occurs in the winter hemisphere, which is also the region of maximum latitudinal variations of insolation, at the edge of the polar night. The same asymmetry persists at equinox, the maximum winds occurring in the hemisphere coming out of winter.

4 Discussion

4.1 Comparison to observations

As already mentioned, the thermal winds deduced from Voyager observations (Flasar et al., 1981) as well as the analysis of the central flash produced during the occultation of 28 Sgr by Titan (Sicardy et al., 1990; Hubbard, 1993) suggest winds of the order of 100 m s^{-1} in the high stratosphere ($p \sim 1 - 0.2$ mbar) in good agreement with our numerical results. However neither of these observations give an indication on the direction of the zonal winds.

[Figure 9 about here.]

The wind profile retrieved from the star occultation by Hubbard *et al.* (1993) is shown in Fig. 9 (squares). The main features are the large equatorial zonal winds of the order of 80-100 m s^{-1} and the presence in each hemisphere of a strong high latitude jet. As mentioned by Hubbard *et al.* (1993), the high-frequency variations in the zonal wind are artifacts of the retrieval technique, in which the atmospheric shape (deduced from the central flash observations) is fitted with Legendre polynomials. The zonal winds simulated by the model at the same season ($L_S \sim 128$) in the same pressure range are also shown in Fig. 9. The agreement is very good for the equatorial winds. On the other hand the intensity of the high-latitude winter jet (southern hemisphere) is underestimated by the model. The simulation also suggests that the assumption of symmetry used to retrieve winds from the star occultation is not valid, the simulated wind being much weaker in the northern (summer) hemisphere than at the edge of the polar night in the southern hemisphere. In fact, the occultation was mainly sensitive to the southern hemisphere since the northern hemisphere was much more opaque because of thick haze (Hubbard *et al.* , 1993, Sicardy, personal communication).

It is also possible to make some direct comparisons to the latitudinal temperature variations observed by Voyager 1. The Voyager encounter corresponds approximately to the northern spring equinox. The latitudinal temperature variations have been retrieved from the IRIS measurement by Flasar et al. (1981) and Flasar and Conrath (1990) for two broad stratospheric layers centered at about 1 and 0.4 mbar, corresponding respectively to the wings and center of the ν_4 methane band. More recently, Coustenis and Bézard (1994) deduced from the same data vertical stratospheric temperature profiles for different latitudes.

Latitudinal temperature variations were small at the time of the the Voyager encounter between 30S and 30N and larger in the 30-60 region in both hemispheres. The mid-northern latitudes (hemisphere coming out of winter) were also found to be significantly colder (by about 6 K at 1 mbar and 15 K at 10 mbar) than the southern mid-latitudes. This result has generally been considered as puzzling since the Voyager observations correspond approximately to equinox and because the radiative time constants are expected to be much shorter than one Titan season (Flasar et al., 1981) . Two explanations have been proposed for this asymmetry: a dynamical origin (Flasar and Conrath, 1990) and a radiative origin due to the latitudinal variations of chemical composition and aerosol content (Bezard et al., 1994) . Note also that all retrievals indicate latitudinal temperature gradients decreasing with altitude in the 10-0.1 mbar region.

[Figure 10 about here.]

Fig. 10 shows the observed and modeled latitudinal temperature variations for two ranges of latitudes: $T_{53S} - T_{50N}$ (upper panel), representative of hemispheric asymmetries, and $T_{24N} - T_{50N}$ (lower panel), corresponding to the region of maximum latitudinal temperature gradients in the observations.

Note that, despite the rather short radiative time constants in the stratosphere, the two-dimensional radiative-convective simulation (without dynamics) produces a significant hemispheric asymmetry. In fact, this asymmetry is surprisingly similar to that observed. On the other hand hemispheric contrast are much smaller in the three-dimensional simulation with dynamics. The same remarks apply to the latitudinal temperature gradients in the northern mid-latitudes: a very good agreement is obtained without dynamics but inclusion of dynamics produces too small latitudinal temperature variations.

4.2 Angular momentum budget and atmospheric superrotation

As first proposed by Gierasch (1975) for Venus, and latter on obtained in numerical simulations (Hourdin et al., 1992; Del Genio et al., 1993; Hourdin and Talagrand, 1994) , a key for the creation and maintenance of atmospheric superrotation is the upward transport of angular momentum by the mean meridional circulation. For a slowly rotating planet with a null obliquity, the mean meridional circulation is dominated by large equator-to-pole Hadley cells. If, in addition, there is more angular momentum in low than at high latitudes (this is the case for example for an atmosphere at rest with respect to the rotating planet), the Hadley cells transport more angular momentum upward in the low latitude ascending branches than in the descending branches in high latitudes. At the same time, for a superrotating atmosphere, more angular momentum is transported poleward in the upper branch of the Hadley cell than equatorward in the lower branch (where the zonal wind is weaker). In the simulations of superrotation mentioned above, this systematic poleward transport is partly compensated by a systematic equatorward transport by transient eddies capable of maintaining an excess of angular momentum in low latitudes. These transient eddies were also shown to be forced by barotropic and inertial unstabilities, forced themselves by the poleward transport of angular momentum by the mean meridional circulation (Hourdin and Talagrand, 1994) .

In the Titan simulation presented here, as in the simulations mentioned above, the annually averaged mean meridional circulation (Fig. 4) is dominated by large equator-to-pole Hadley cells. Since at the same time, angular momentum decreases from equator to pole (not shown), the mean meridional circulation, as explained above, results in a net upward flux of angular momentum. This total upward transport of (dimensionless) angular momentum by the annually averaged mean meridional circulation is shown in Fig. 11 (circles) for the troposphere (upper panel) and stratosphere (lower panel).

[Figure 11 about here.]

In the various simulations of superrotation mentioned above, the superrotation increased until an equilibrium was reached between upward transport by the mean meridional circulation and downward transport by the parametrized vertical turbulent mixing. The situation is equivalent in Titan's troposphere but not in the stratosphere where the parametrized vertical mixing has a negligible effect on the angular momentum balance (not shown). In fact the annually averaged circulation hides strong seasonal contrasts. Near equinox, when the mean meridional circulation is almost symmetric with respect to the equator, the mean meridional circulation transports angular momentum upward (triangles in Fig. 11) both in the troposphere (upper panel) and stratosphere (lower panel) but at solstice in the stratosphere, the zonal wind is stronger in the winter hemisphere, *i. e.* in the descending branch of the pole-to-pole Hadley cell, resulting in a downward transport of angular momentum in the stratosphere (crosses in Fig. 11). Thus in the stratosphere, the superrotation stops increasing when the downward transport by the mean meridional circulation at solstice balances the upward transport at equinox. As a consequence, note that the intensity of the stratospheric superrotation must not depend significantly on the values chosen for the parameters controlling the vertical diffusion. This seasonal variations of the vertical transport of angular momentum in the stratosphere also explain the seasonal oscillations shown in Fig. 2 and Fig. 3 with a maximum of angular momentum between equinox and solstice in the upper stratosphere.

As in the other simulations of superrotation also, the poleward transport of angular momentum by the Hadley circulation in the upper branch of the Hadley cell is compensated in part by a systematic equatorward transport by transient eddies as illustrated in Fig. 12.

[Figure 12 about here.]

But once again, as for the vertical transport, the annual mean hides a strong seasonal cycle. At northern winter solstice (upper panel of Fig. 13), the transport by the mean meridional circulation is northward in both hemispheres whereas it is much smaller in the southern hemisphere at northern spring equinox (lower panel) and almost null in the northern hemisphere. The transport by transient eddies is southward (opposite to the mean meridional circulation) near solstice and almost null near equinox.

[Figure 13 about here.]

Note also that transport by the parametrized horizontal dissipation is negligible everywhere except in very high latitudes.

In summary, the simple picture of the creation and maintenance of superrotation deduced from more theoretical simulations of atmospheric superrotation can be applied for Titan especially for the troposphere. In the stratosphere, the mechanism is the same on an annual basis but hides more complex seasonal behaviors.

4.3 Temperature

As mentioned above, the model produces too small latitudinal temperature gradients by comparison to Voyager data. At the same time, the observed latitudinal temperature variations are remarkably well simulated without dynamics with the two-dimensional radiative-convective version of the model. As already said also, the atmospheric dynamics are expected to reduce the "radiative" latitudinal temperature gradients, especially for slowly rotating planets (Del Genio et al., 1983; Del Genio et al., 1993; Hourdin and Talagrand, 1994) . In the present simulation, the latitudinal temperature gradients in the upper branch of the Hadley cell are reduced by a very efficient poleward transport of energy by the mean meridional circulation (as illustrated in Fig. 14) whereas transient eddies play a minor role.

[Figure 14 about here.]

At least two explanations can be proposed for the discrepancy between model and observations. First, the latitudinal and seasonal variations of the radiative forcing could be underestimated since the spatial and temporal variations of the chemical composition and haze abundance are not accounted for in the model. Recent studies indeed suggest that the hemispheric differences of aerosol content and radiatively active chemical species could produce strong hemispheric asymmetries in the radiative heating and cooling rates (Bezard et al., 1994) . Another explanation could be that some dynamical effects are not accounted for in the model such as the possible effect of gravity waves, major component of the terrestrial stratospheric dynamics. The presence of such waves on Titan is suggested, below 100 km by the scintillation of the radio-signal during the occultation of Voyager 1 by Titan (Friedson, 1994) and, between 280 and 470 km, where they would have amplitudes similar to terrestrial gravity waves, by the results of the 28-Sgr occultation (Sicardy, personal communication).

Both hypotheses require appropriate tests. Performing such tests is however rather challenging. The inclusion of latitudinal variations of chemical composition and haze would require (in view of the poor observational knowledge we have) the development of a coupled chemical-aerosol-model. On the other hand, parametrization of the effect of gravity waves in the model requires to specify sources for those waves which is an unsolved problem even for the much better known terrestrial circulation.

It is also possible that a finer horizontal discretization could help to increase the simulated latitudinal temperature gradients, as was observed when passing from the low to high resolution. However, we essentially attribute the latter difference to the fact that horizontal dissipation has too large an impact for the low resolution whereas it does not affect directly temperature for the high resolution simulation presented here. Anyway, it is difficult to believe that a change of horizontal resolution alone will almost cancel the effect of the reduction of the latitudinal temperature gradients by the dynamics.

5 Conclusion

We have presented the first self-consistent numerical simulations of the atmospheric general circulation of Titan. The main result is the creation by the model of a strong atmospheric superrotation. The values of the zonal wind in the stratosphere (of the order of 100 m s^{-1} near the 1 mbar level) are consistent with the results from the star-occultation. Moreover, the model predicts prograde winds everywhere, except in low latitude in the lower troposphere, with an atmosphere rotating about 8 times faster than the solid planet near 1 mbar, and 2-3 times faster at the tropopause level.

The model also predicts a strong seasonal cycle of the zonal wind in the stratosphere, with rather weak winds in the range 40-70 m s^{-1} in the winter hemisphere (the asymmetry persisting at equinox).

However important disagreements exist with Voyager observations as far as latitudinal thermal contrasts are concerned. The disagreement may be due to the lack of representation of the seasonal changes in the abundance of radiatively active chemical species and haze which have been shown to strongly influence the radiative budget (Bezard et al., 1994) . It appears to be necessary to develop for Titan a coupled model including dynamics, aerosol physics and chemistry. A first step has recently been made in that direction by Hutzell et al. (1994) who have introduced the seasonally varying mean meridional circulation as simulated with our GCM in a 2-D model of the physics of Titan's aerosols.

References

Barnes, J. R., J. B. Pollack, R. M. Haberle, R. W. Zurek, C. B. Leovy, H. Lee, and J. Schaeffer, 1993, Mars atmospheric dynamics as simulated by the NASA/Ames general circulation model II. transient baroclinic eddies, *J. Geophys. Res.*, *98*, (E2), 3125–3148.

Bezard, B., A. Coustenis, and C. P. McKay, Titan's stratospheric temperature asymmetry: a radiative origin, submitted to *Icarus*, 1994.

Broadfoot, A. L., M. J. S. Belton, P. Z. Takacs, B. R. Sandel, D. E. Shemansky, J. B. Holberg, J. M. Ajello, S. K. Atreya, T. M. Donahue, H. W. Moos, J. L. Bertaux, J. E. Blamont, D. F. Strobel, J. C. McConnell, A. Dalgarno, R. Goody, and M. B. McElroy, 1981, Extreme ultraviolet observations from Voyager 1 encounter with Saturn, *Science*, *212*, 206–211.

Caldwell, J., C. C. Cunningham, D. Anthony, H. P. White, E. J. Groth, H. Hasan, K. Noll, P. H. Smith, M. G. Tomasko, and H. A. Weaver, 1992, Titan: Evidence for seasonal change — a comparison of Hubble Space Telescope and Voyager images, *Icarus*, *96*, 1–9.

Courtin, R., 1988, Pressure induced absorption coefficients for radiative transfer in Titan's atmosphere, *Icarus*, *75*, 245–254.

Coustenis, A., and B. Bézard, Titan's atmosphere from Voyager infrared observations: IV latitudinal variations of temperature and composition, submitted for publication, 1994.

Del Genio, A. D., J. K. Meccage, R. Suozzo, R. Opstbaum, D. Rind, W. B. Rossow, G. Russel, and L. D. Travis, 1983, Variable rotation rate experiments with the GISS general circulation model, *Bull. Am. Astron. Soc.*, *15*, 821.

Del Genio, A. D., W. Zhou, and T. P. Eichler, 1993, Equatorial superrotation in a slowly rotating GCM: implications for Titan and Venus, *Icarus*, *101*, 1–17.

Flasar, F. M., and B. J. Conrath, 1990, Titan's stratospheric temperatures: a case for dynamical inertia?, *Icarus*, *85*, 346–354.

Flasar, F. M., R. E. Samuelson, and B. J. Conrath, 1981, Titan's atmosphere: temperature and dynamics, *Nature*, *292*, 693–698.

Friedson, A. J., 1994, Gravity waves in Titan's atmosphere, *Icarus*, *109*, 40–57.

Gierasch, P. J., 1975, Meridional circulation and the maintenance of the Venus atmospheric rotation, *J. Atmos. Sci.*, *32*, 1038–1044.

Golitsyn, G. S., 1975, Another look at atmospheric dynamics on Titan and some of its general consequences, *Icarus*, *24*, 70–75.

Haberle, R. M., J. B. Pollack, J. R. Barnes, R. W. Zurek, C. B. Leovy, J. R. Murphy, H. Lee, and J. Schaeffer, 1993, Mars atmospheric dynamics as simulated by the NASA/Ames general circulation model I. the zonal-mean circulation, *J. Geophys. Res.*, *98*, (E2), 3093–3124.

Holton, J. R., 1979, *An introduction to dynamic meteorology*, A. L. Hales (Ed.), vol. 23 of *Internal geophysics series*, Academic Press, second edition.

Hourdin, F., and O. Talagrand, Superrotation of planetary atmospheres: a numerical study, submitted to J. Atmosph. Sci., 1994.

Hourdin, F., P. Le Van, O. Talagrand, R. Courtin, D. Gautier, and C. McKay, 1992, Numerical simulation of the circulation of the atmosphere of Titan, in *Symposium on Titan*, edited by ESA, vol. SP-338, 101–106, ESA.

Hourdin, F., P. Le Van, F. Forget, and O. Talagrand, 1993, Meteorological variability and the annual surface pressure cycle on Mars, *J. Atmos. Sci.*, *50*, 3625–3640.

Hourdin, F., F. Forget, and O. Talagrand, The sensitivity of the Martian surface pressure to various parameters: a comparison between numerical simulations and Viking observations, submitted to J. Geophys. Res., 1994.

Hourdin, F., 1992, A new representation of the CO_2 15μm band for a Martian general circulation model, *J. Geophys. Res.*, *97*, (E11), 18,319–18,335.

Hubbard, W. B. *et al.* , 1993, The occultation of 28 sgr by titan, *Astron. Astrophys.*, *269*, 541–563.

Hunten, D., M. G. Tomasko, F. M. Flasar, R. E. Samuelson, D. F. Strobel, and D. J. Stevenson, 1984, Titan, in *Saturn*, 671–759, Univ. of Arizona Press, Tucson.

Hutzell, W. T., C. P. McKay, O. B. Toon, and F. Hourdin, Simulations of Titan's brightness by a two-dimensional haze model, submitted to *Icarus*, 1994.

Kasahara, A., 1977, Computational aspects of numerical models for weather prediction and climate simulation, in *Methods in computational physics*, edited by J. Chang, vol. 17, 1–66, Academic press, inc.

Khare, B. N., C. Sagan, E. T. Arakawa, F. Suits, T. A. Callcott, and M. W. Williams, 1984, Optical constants of organic tholins produced in a simulated Titanian atmosphere: from soft X-ray to microwave frequencies, *Icarus*, *60*, 127–137.

Kunde, V. G., A. C. Aikin, R. A. Hanel, D. E. Jennings, W. C. Maguire, and R. E. Samuelson, 1981, C_4H_2, HC_3N and C_2N_2 in Titan's atmosphere, *Nature*, *292*, 686–688.

Lellouch, E., A. Coustenis, D. Gautier, F. Raulin, N. Dubouloz, and C. Frère, 1989, Titan's atmosphere and hypothesized ocean: A reanalysis of Voyager 1 radio-occultation and IRIS 7.7 μm data., *Icarus*, *79*, 328–349.

Leovy, C. B., G. A. Briggs, and B. A. Smith, 1973, Mars atmosphere during the Mariner 9 extended mission: Television results, *J. Geophys. Res.*, *78*, 4252–4266.

Lindal, G. F., G. E. Wood, H. B. Hotz, D. N. Sweetnam, V. R. Eshleman, and G. L. Tyler, 1983, The atmosphere of Titan: an analysis of the Voyager 1 radio occultation measurements, *Icarus*, *53*, 348–363.

Lockwood, G. W., B. L. Lutz, D. T. Thompson, and E. S. Bus, 1986, The albedo of Titan, *Astrophys. J.*, *303*, 511–520.

Lockwood, G. W., 1977, Secular brightness increase of Titan, Uranus, Neptune 1972–1976, *Icarus*, 413–430.

McKay, C. P., J. B. Pollack, and R. Courtin, 1989, The thermal structure of Titan's atmosphere, *Icarus*, *80*, 23–53.

McKay, C. P., J. B. Pollack, and R. Courtin, 1991, The greenhouse antigreenhouse effects on Titan, *Science*, *253*, 1118–1121.

McKay, C. P., J. B. Pollack, J. I. Lunine, and R. Courtin, 1993, Coupled atmosphere-ocean models of Titan's past, *Icarus*, *102*, 88–98.

Pedlosky, J., 1982, *Geophysical Fluid Dynamics*, Springer-Verlag, New York.

Pollack, J. B., C. B. Leowy, P. W. Greiman, and Y. Mintz, 1981, A Martian General Circulation Model experiment with large topography, *J. Atmos. Sci.*, *38*, 3–29.

Pollack, J. B., R. M. Haberle, J. R. Murphy, J. Shaeffer, and H. Lee, 1993, Simulation of the general circulation of the Martian atmosphere II: seasonnal pressure variations, *J. Geophys. Res.*, *98*, (E2), 3149–3181.

Rages, K., and J. B. Pollack, 1983, Vertical distribution of scattering hazes in Titan's upper atmosphere, *Icarus*, *55*, 50–62.

Rages, K., J. B. Pollack, and P. H. Smith, 1983, Size estimates of Titan's aerosols based on Voyager high-phase-angle images, *J. Geophys. Res.*, *88*, 8721–8728.

Sadourny, R., and K. Laval, 1984, January and july performance of the LMD general circulation model, in *New perspectives in Climate Modeling*, edited by A Berger and C.Nicolis, number 16 in Elsevier Sc., 173–197, Cy.

Sadourny, R., 1975*a*. Compressible model flows on the sphere, *J. Atmos. Sci.*, *32*, 2103–2110.

Sadourny, R., 1975*b*, The dynamics of finite-difference models of the shallow-water equations, *J. Atmos. Sci.*, *32*, 680–689.

Sagan, C., and W. R. Thompson, 1984, Production and condensation of organic gases in the atmosphere of Titan, *Icarus*, *59*, 133–161.

Samuelson, R. E., R. A. Hanel, V. G. Kunde, and W. C. Maguire, 1981, Mean molecular weight and hydrocarbon abundance of Titan's atmosphere, *Nature*, *292*, 688–693.

Sicardy, B., A. Brahic, C. Ferrari, D. Gautier, J. Lecacheux, E. Lellouch, F. Roques, J. E. Arlot, F. Colas, W. Thuillot, F. Sèvre, J. Vidal, C. Blanco, S. Cristaldi, C. Buil, A. Klotz, and E. Thouvenot, 1990, Probing Titan's atmosphere by stellar occultation, *Nature*, *343*, 350.

Sromovsky, L. A., V. E. Suomi, J. B. Pollack, R. J. Kraus, S. S. Limaye, T. Owen, H. E. Revercomb, and K. Sagan, 1981, Implications of Titan's north-south brightness asymmetry, *Nature*, *292*, 698–702.

Strobel, D. F., H. D. T., X. Zhu, and M. E. Summers, 1993, Upper limit on Titan's atmospheric argon abundance, *Icarus*, *103*, 333–336.

Toon, O. B., C. P. McKay, T. P. Ackerman, and K. Santhanam, 1989, Rapid calculation of radiative heating rates and photodissociation rates in inhomogeneous multiple scattering atmospheres, *J. Geophys. Res.*, *94*, (D13), 16,287–16,301.

Tourte, J.-L., 1984, *Modélisation numérique de la circulation de l'atmosphère de Vénus*, Thèse de docteur -ingénieur, Université Pierre et Marie Curie, Paris.

Young, R. E., and J. B. Pollack, 1990, A three-dimensional model of dynamical processes in the Venus atmosphere, *J. Atmos. Sci.*, *34*, 1315–1351.

List of Figures

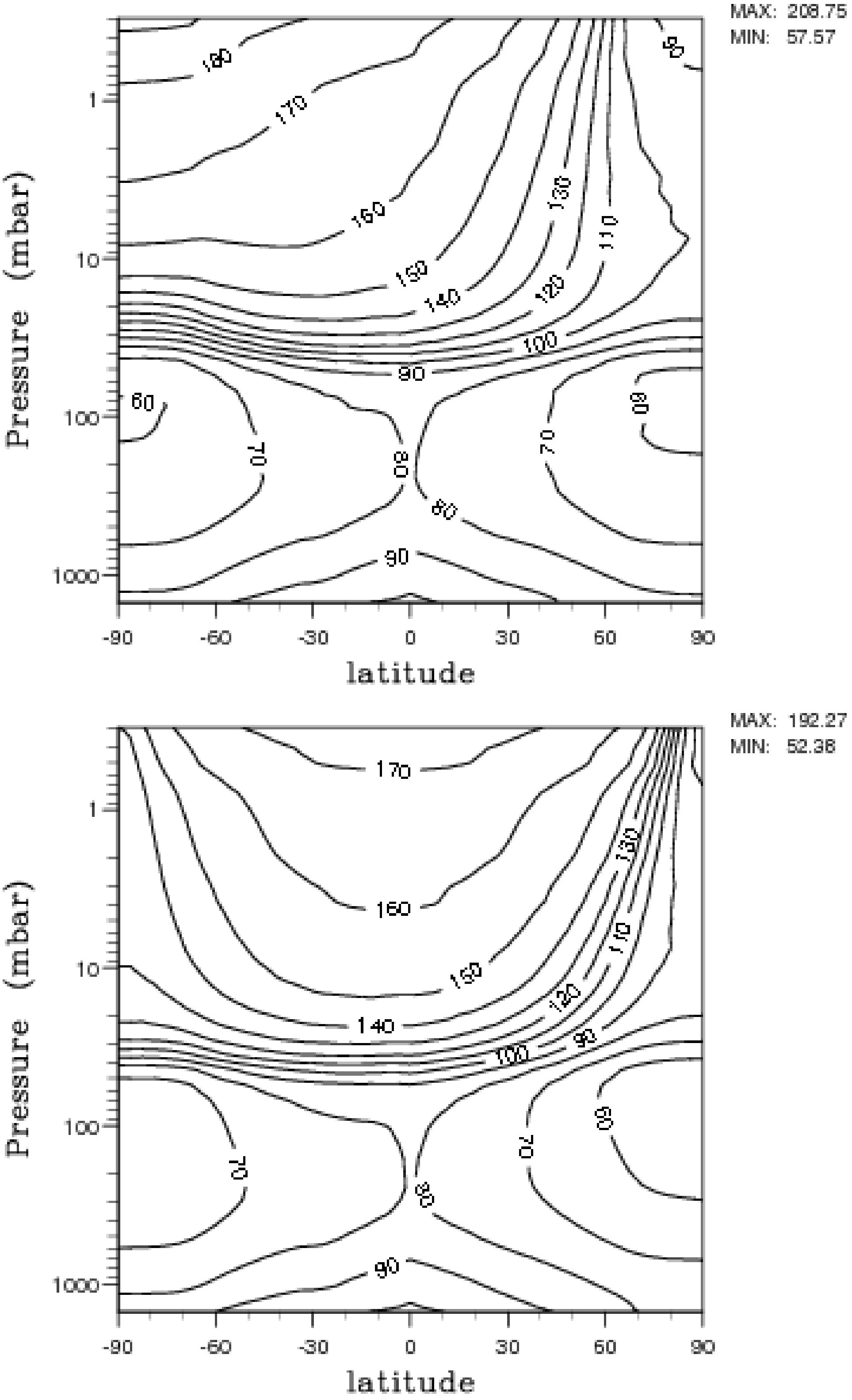

Figure 1: Temperature at northern winter solstice (upper panel) and spring equinox (lower panel) computed with a 2-D (latitude-altitude) radiative-convective version of the GCM, with seasonal and latitudinal variations of insolation.

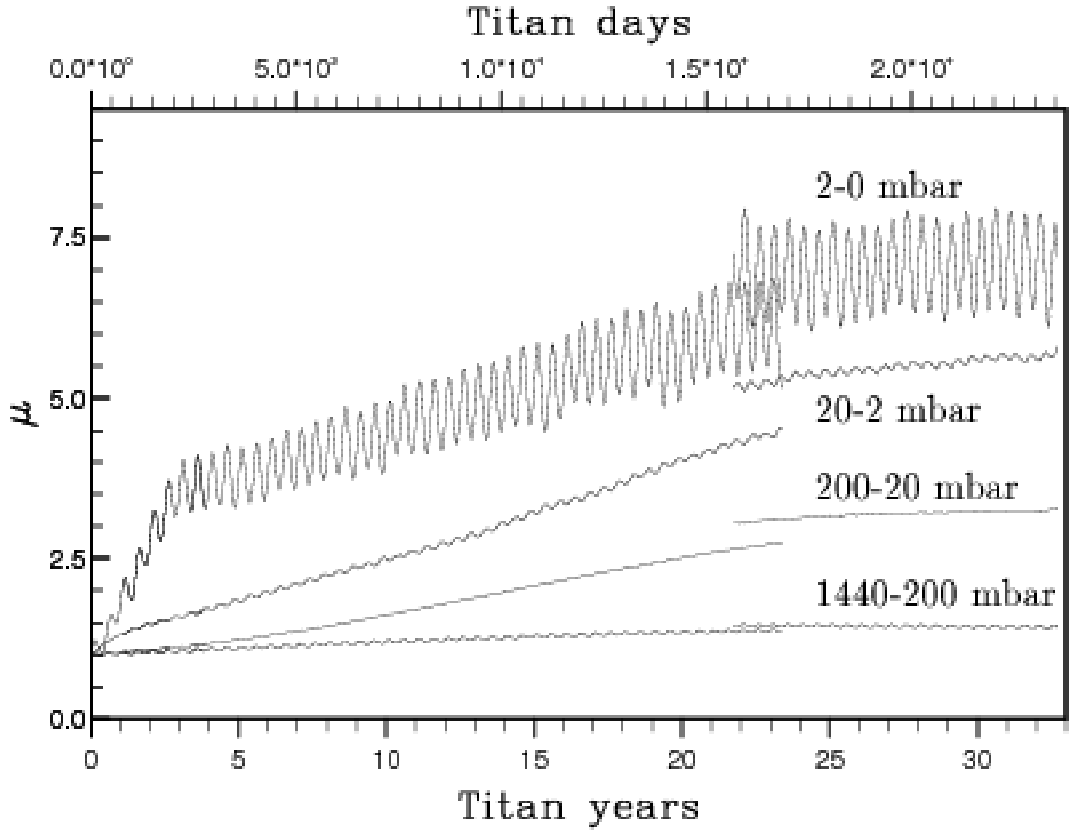

Figure 2: Time evolution of the planetary averaged of the dimensionless angular momentum μ

$$\mu = \frac{3}{2\Omega a} \cos\phi \, (u + a\Omega \cos\phi) \tag{4}$$

for four atmospheric layers in the low resolution simulation.

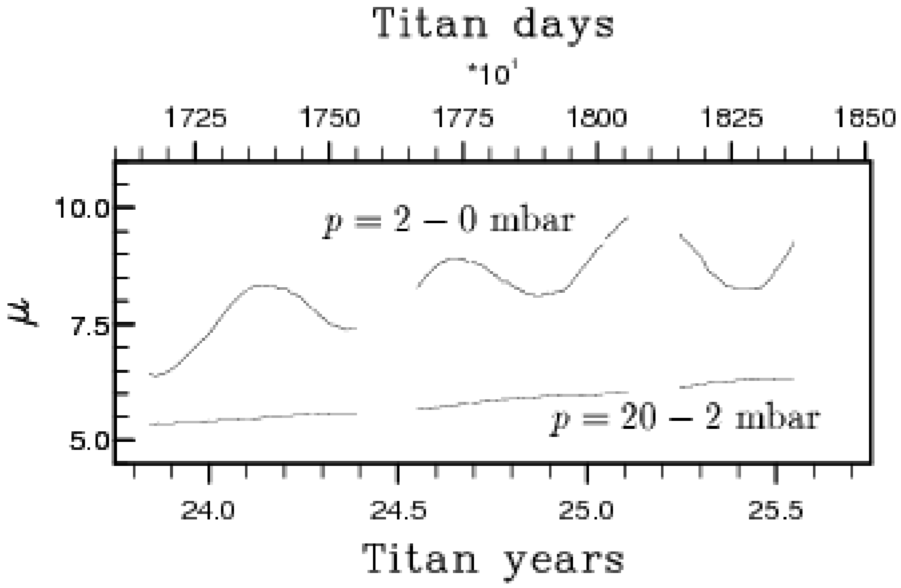

Figure 3: Time evolution of the planetary average of the dimensionless angular momentum in the stratosphere as simulated with the high horizontal resolution.

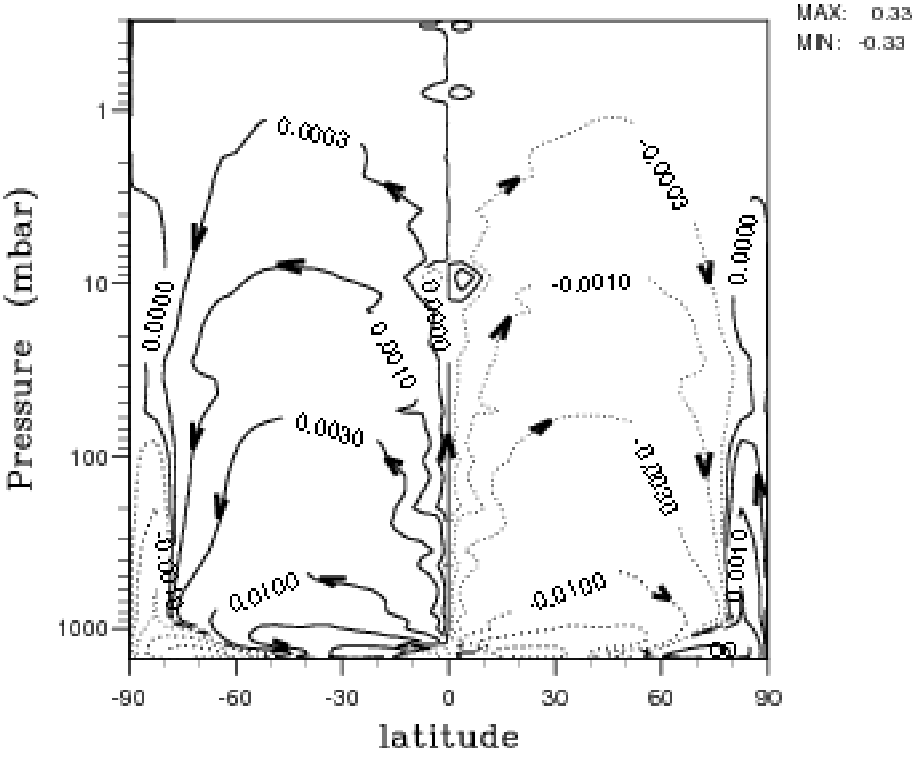

Figure 4: Stream function of the annually and zonally averaged meridional circulation (kg s^{-1}).
The difference between two iso-values is equal to the mass flux across a meridional section comprised between the two corresponding iso-lines. The direction of the circulation is given by the small arrows.

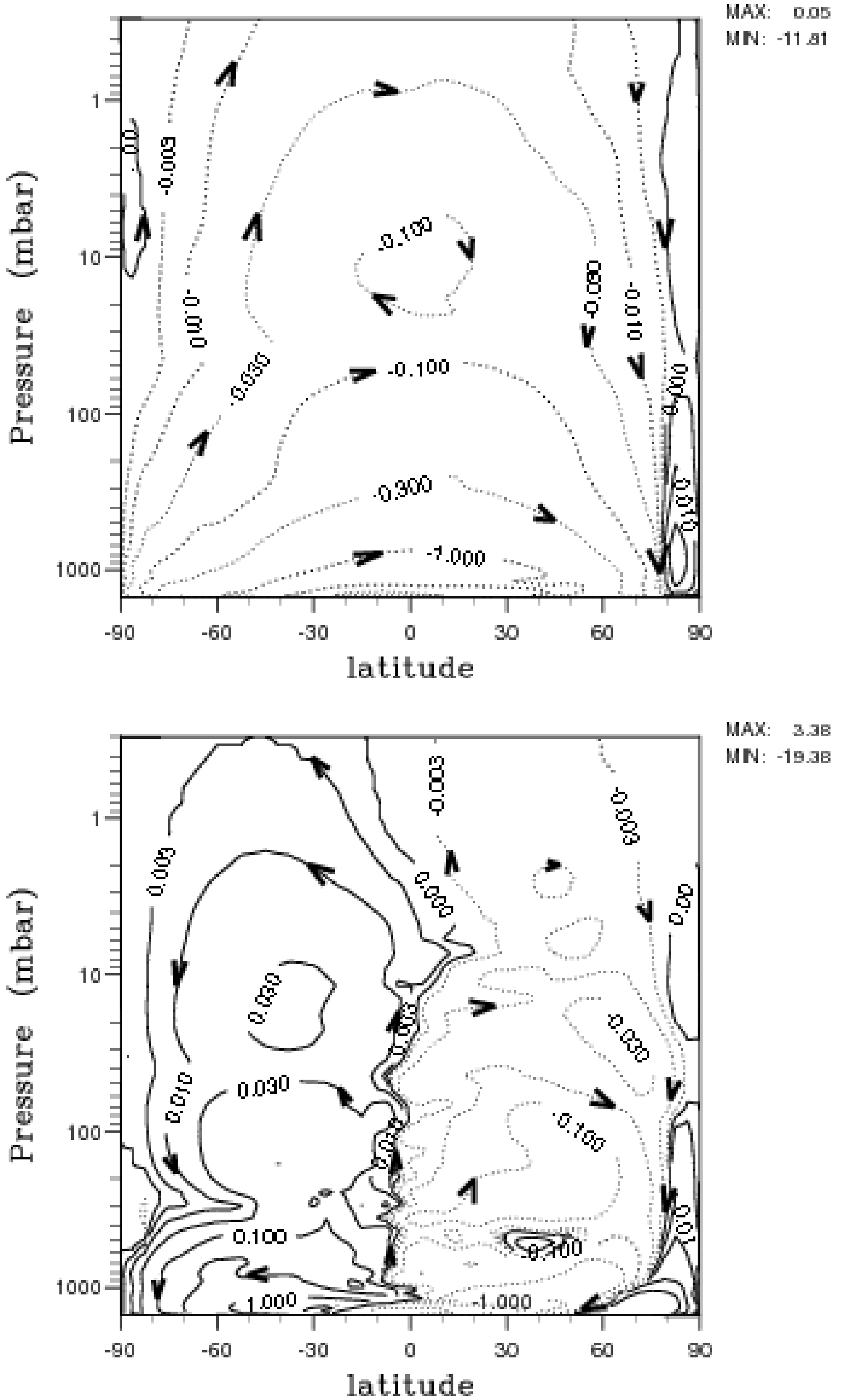

Figure 5: Stream function of the zonally averaged meridional circulation (kg s^{-1}) for northern winter solstice (upper panel) and northern spring equinox (lower panel).

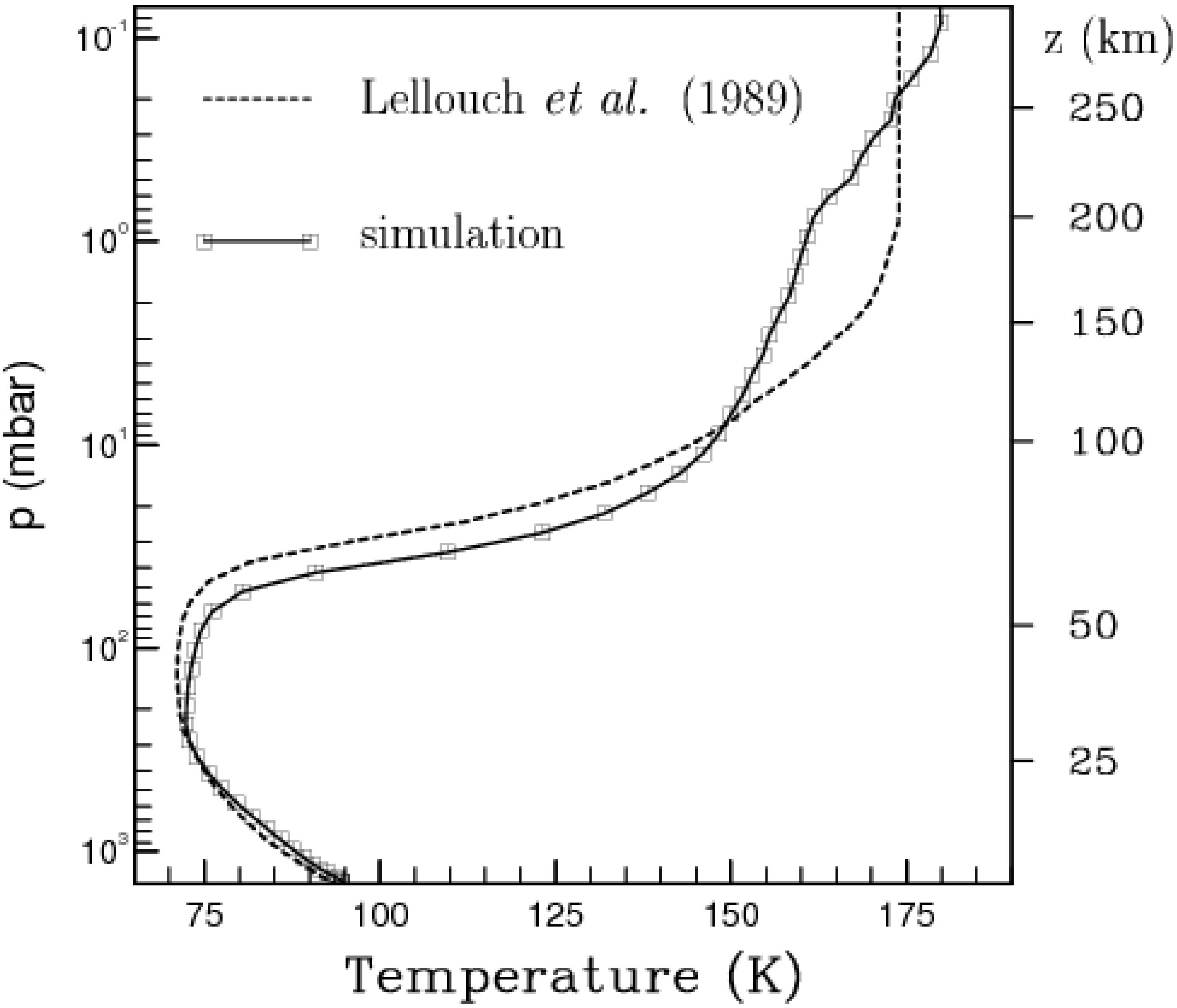

Figure 6: Globally averaged vertical temperature (K) profile as simulated by the GCM (the squares correspond to the model levels) and as deduced from the Voyager data reanalysis by Lellouch *et al.* (1989).

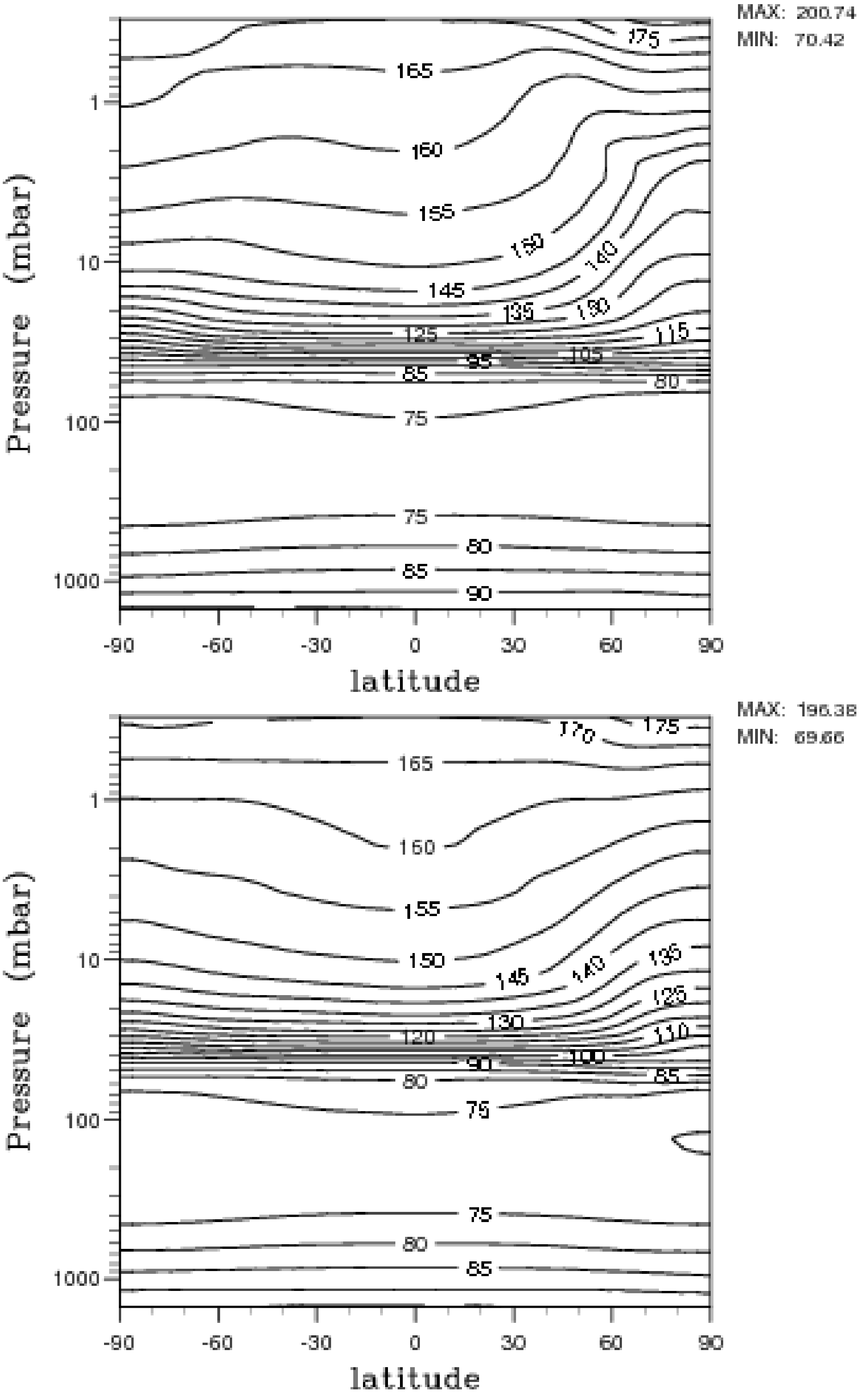

Figure 7: Simulated zonally averaged temperature (K) at northern winter solstice (upper panel) and northern spring equinox (lower panel).

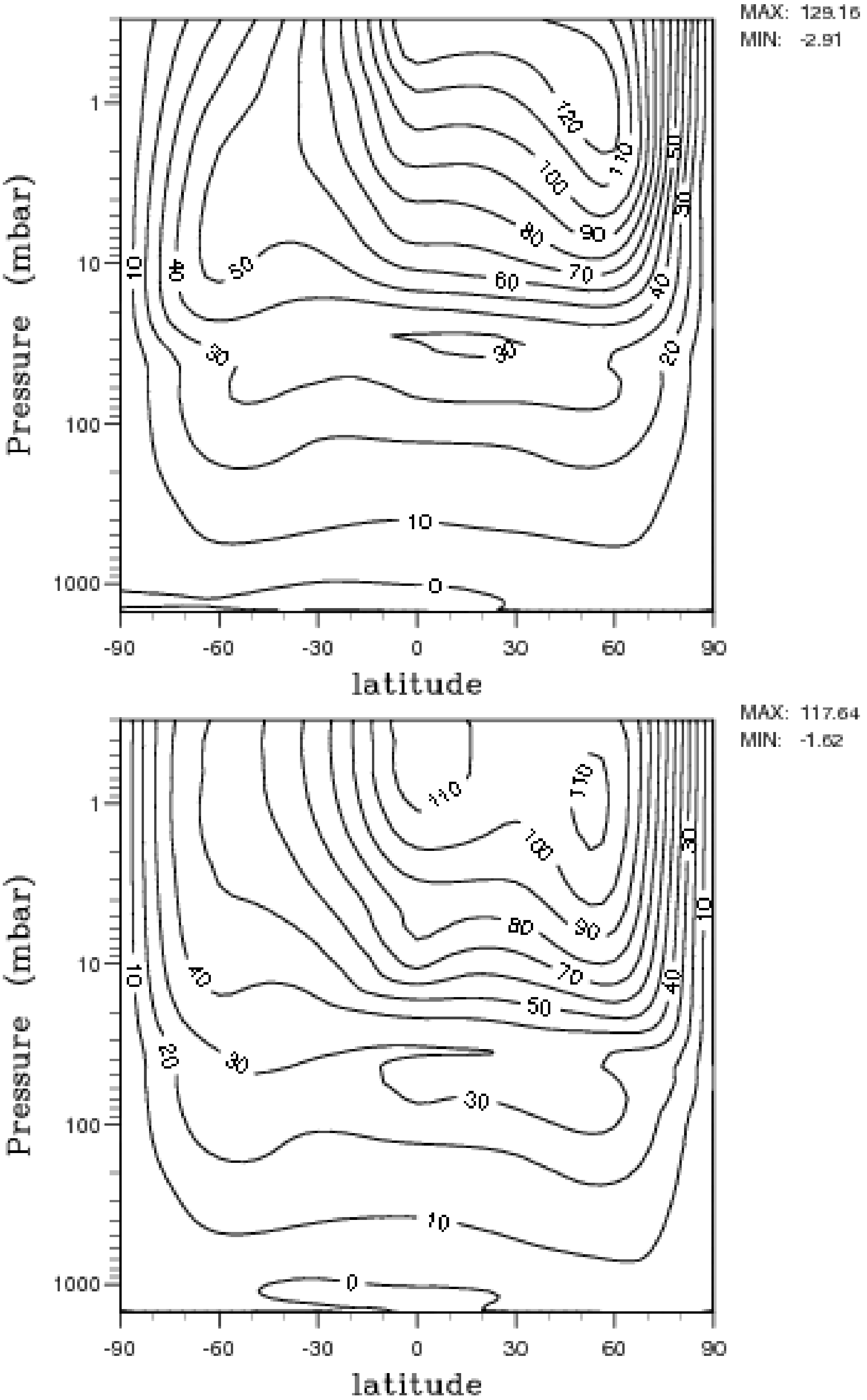

Figure 8: Simulated zonally averaged zonal wind (m s^{-1}) at northern winter solstice (upper panel) and northern spring equinox (lower panel).

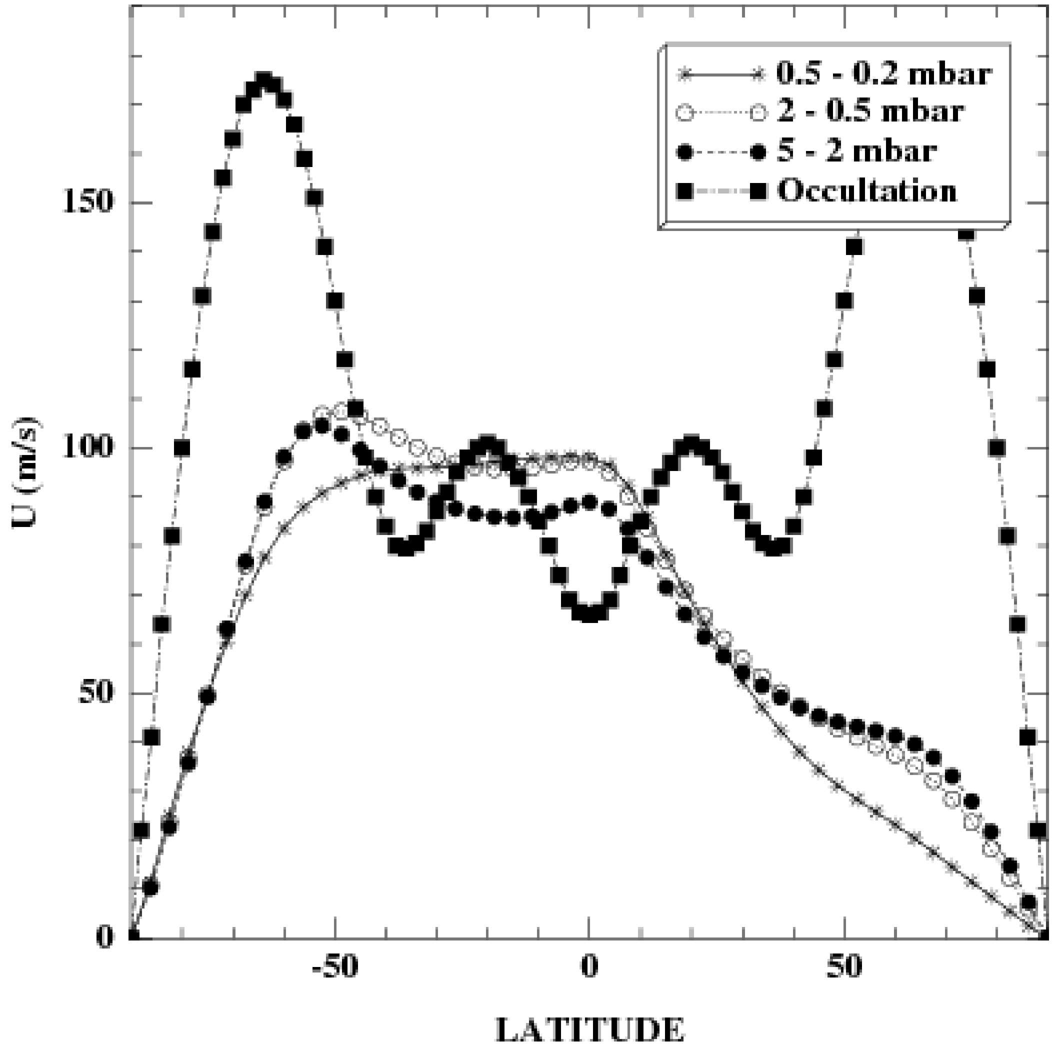

Figure 9: Latitudinal zonal wind profile deduced by Hubbard *et al.* (1993) from the 28-Sgr occultation which corresponds to a pressure level near 0.25 mbar (squares). The other three curves show the zonally averaged zonal wind as produced by the GCM for the same season ($L_S \sim 128$) and for three pressure ranges.

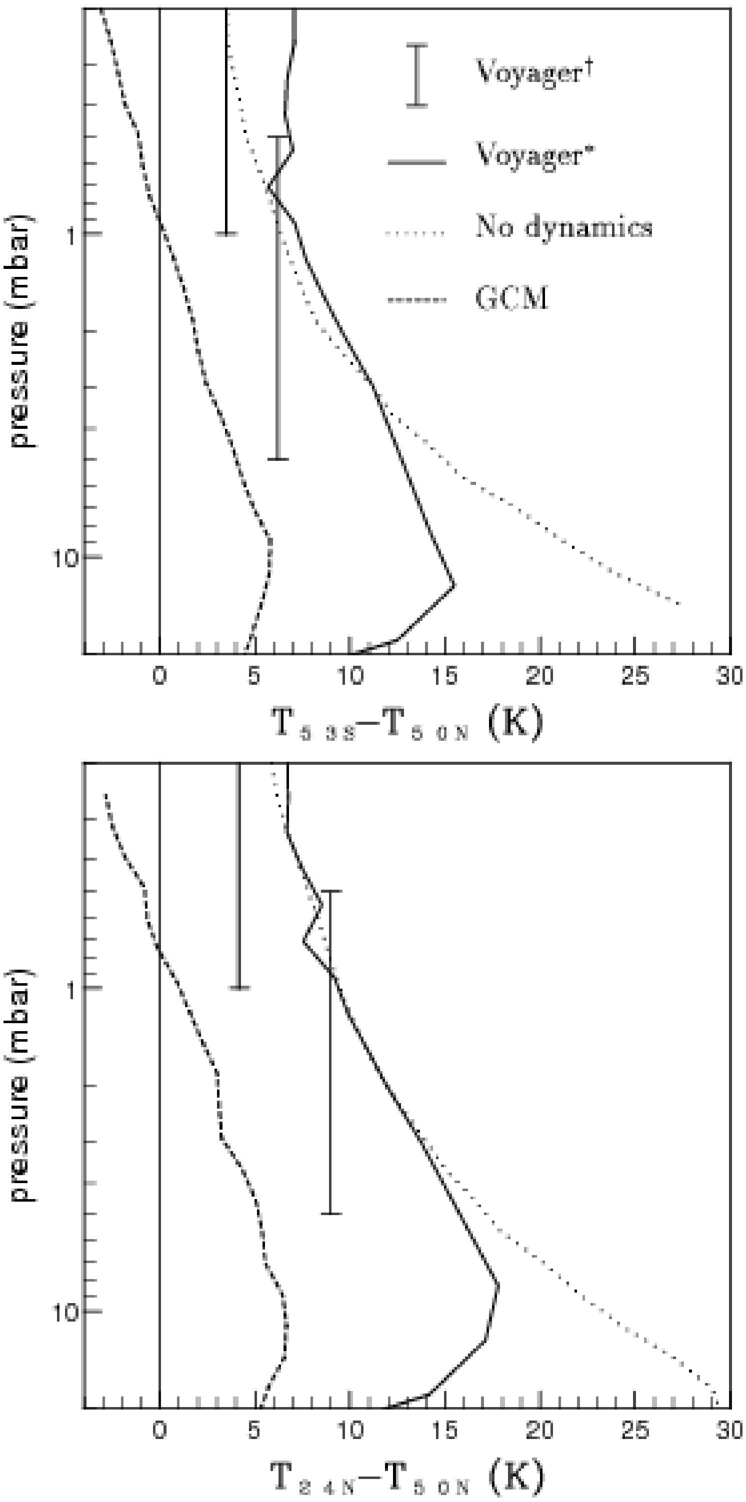

Figure 10: Vertical profile of the temperature difference between two latitudes: 53S and 50N (upper panel) and 24N and 50N (lower panel).
Comparison of the temperature retrieved from the observation of the infra-red emission in the center and wings of the ν_4 CH_3 band by Voyager 1 (†, Flasar and Conrath, 1990, *, Coustenis and Bézard, 1994) and the GCM results with and without dynamics.

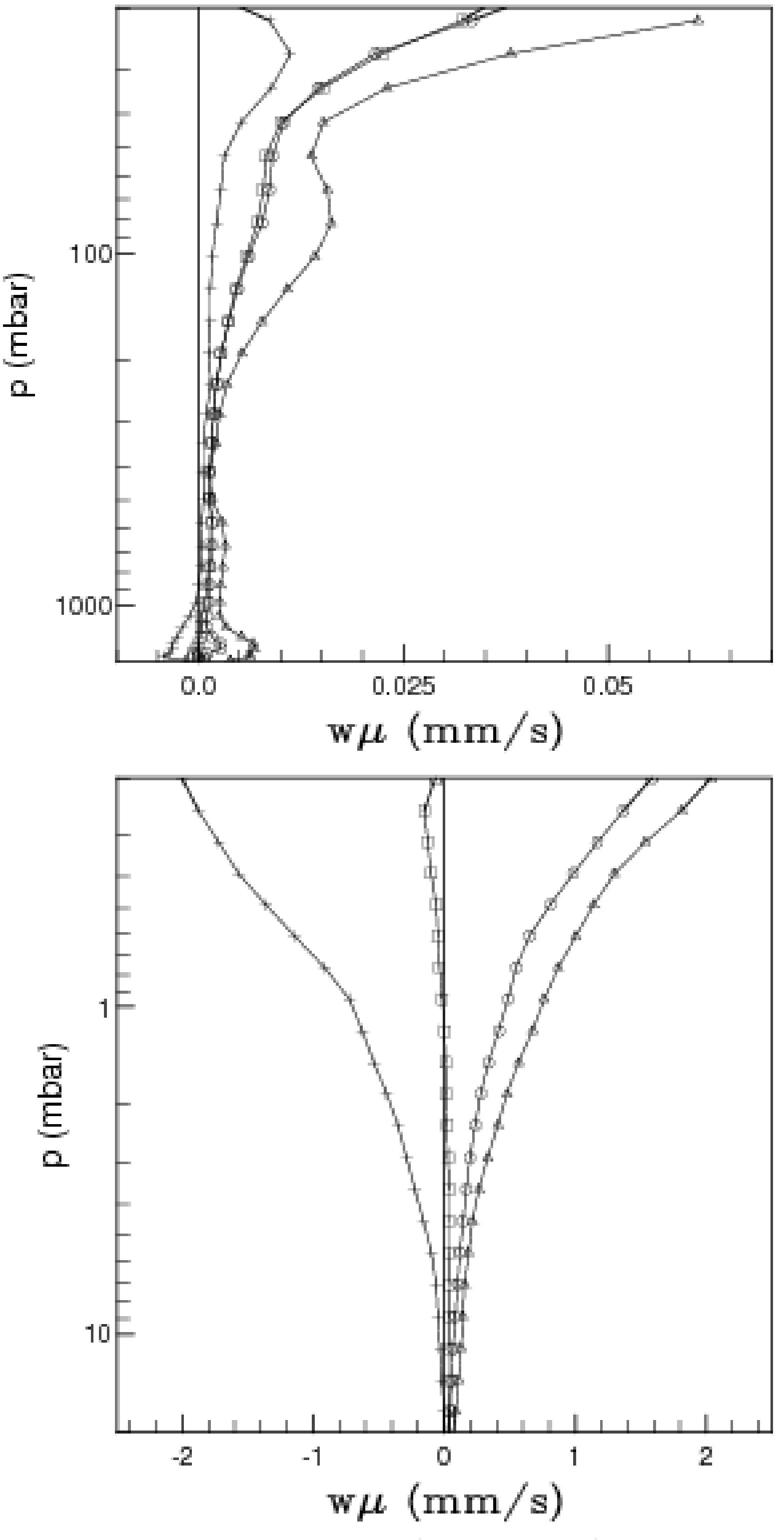

Figure 11: Mean upward transport of (dimensionless) angular momentum by the mean meridional circulation. **(1) Circles:** transport of the annually averaged angular momentum by the annual mean of the meridional circulation. **(2) Triangles:** transport by the mean meridional circulation near equinox. **(3) Crosses:** solstice. **(4) squares:** annual mean of the mean meridional transport. The upper and lower panel correspond to the troposphere and stratosphere respectively.

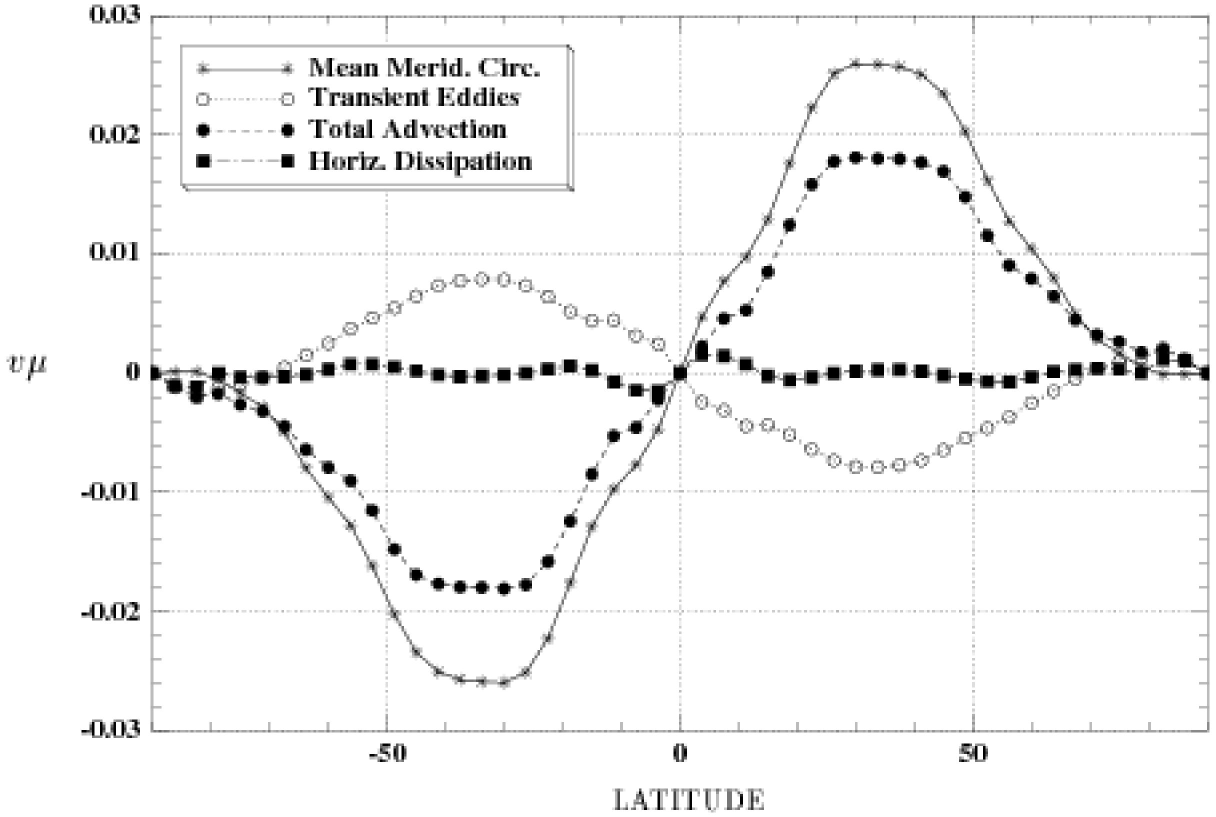

Figure 12: Annual mean of the northward transport of (dimensionless) angular momentum ($v\mu$ in m s^{-1}) by the various components of the atmospheric circulation: transport by the mean meridional circulation, by transient eddies, and the parametrized exchange with subgrid scales (horizontal dissipation). The total advection is very close to the sum of the transport by the mean meridional circulation and transient eddies.

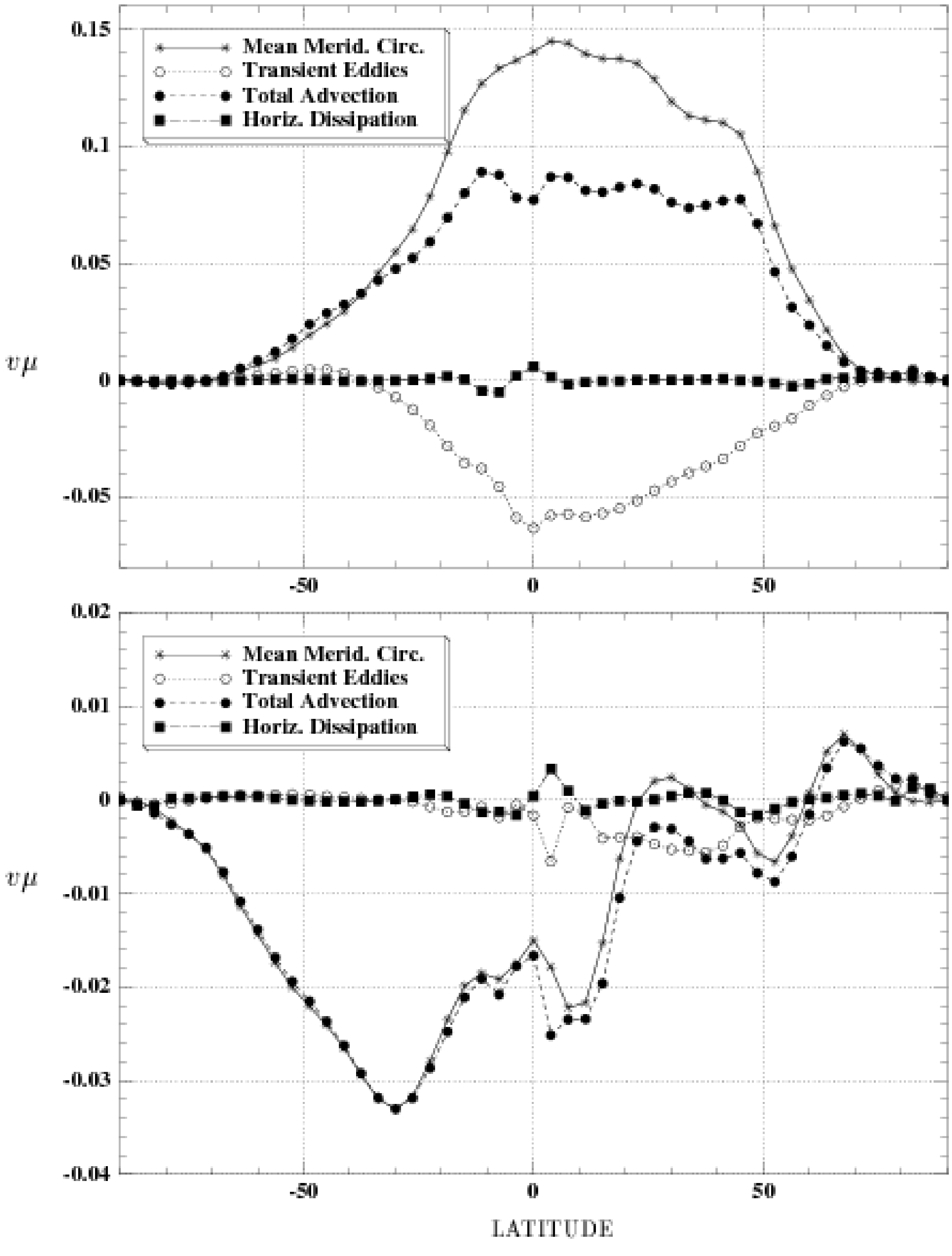

Figure 13: Northward transport of (dimensionless) angular momentum ($v\mu$ in m s^{-1}) at northern winter solstice (upper panel) and northern spring equinox (lower panel) See Fig. 12.

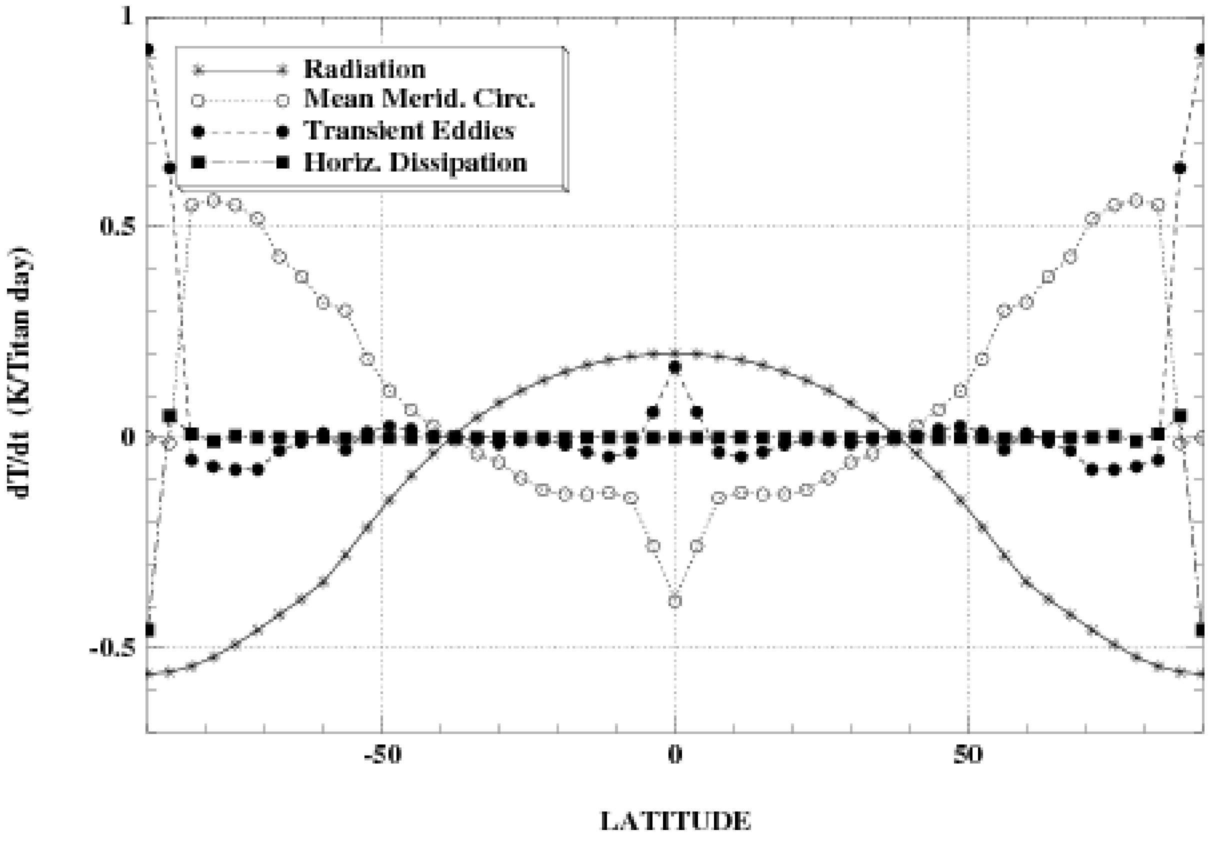

Figure 14: Time derivative of the temperature in the 7-0 mbar region as due to the radiation, transport by the mean meridional circulation and transient eddies and parametrized interaction with subgrid-scales motions (horizontal dissipation).